Monthly Notices of the ROYAL ASTRONOMICAL SOCIETY

MNRAS **541,** 1851–1865 (2025) https://doi.org/10.1093/mnras/staf1098
Advance Access publication 2025 July 7

The accretion–ejection connection in the black hole X-ray binary MAXI J1820+070

Joe S. Bright [1,2★] Rob Fender,[1,3] David M. Russell,[4] Sara E. Motta,[5] Ethan Man,[1] Jakob van den Eijnden [1,6,7] Kevin Alabarta [4] Justine Crook-Mansour,[1] Maria C. Baglio,[5] David A. Green [8] Ian Heywood,[1,2,9,10] Fraser Lewis,[11,12] Payaswini Saikia,[4] Paul F. Scott[8] and David J. Titterington[8]

[1]*Astrophysics, Department of Physics, University of Oxford, Keble Road, Oxford OX1 3RH, UK*
[2]*Breakthrough Listen, Astrophysics, Department of Physics, University of Oxford, Keble Road, Oxford OX1 3RH, UK*
[3]*Department of Astronomy, University of Cape Town, Private Bag X3, Rondebosch 7701, South Africa*
[4]*Center for Astrophysics and Space Science (CASS), New York University Abu Dhabi, PO Box 129188, Abu Dhabi, UAE*
[5]*Istituto Nazionale di Astrofisica, Osservatorio Astronomico di Brera, via E. Bianchi 46, 23807 Merate (LC), Italy*
[6]*Department of Physics, University of Warwick, Coventry CV4 7AL, UK*
[7]*Anton Pannekoek Institute for Astronomy, Universiteit van Amsterdam, Science Park 904, 1098 XH Amsterdam, the Netherlands*
[8]*Astrophysics Group, Cavendish Laboratory, University of Cambridge, Cambridge CB3 0HE, UK*
[9]*Department of Physics and Electronics, Rhodes University, PO Box 94, Makhanda 6140, South Africa*
[10]*South African Radio Astronomy Observatory, 2 Fir Street, Black River Park, Observatory 7925, South Africa*
[11]*Faulkes Telescope Project, Cardiff, Wales, UK*
[12]*The Schools' Observatory, Astrophysics Research Institute, Liverpool John Moores University, 146 Brownlow Hill, Liverpool L3 5RF, UK*

Accepted 2025 June 27. Received 2025 June 23; in original form 2025 March 23

ABSTRACT

The black hole X-ray binary MAXI J1820+070 began its first recorded outburst in March 2018, and remained an active radio, X-ray, and optical source for over 4 yr. Due to the low distance to the source and its intrinsically high luminosity MAXI J1820+070 was observed extensively over this time period, resulting in high-cadence and quasi-simultaneous observations across the electromagnetic spectrum. These data sets provide the opportunity to probe the connection between accretion and the launch of jets in greater detail than for the majority of black hole X-ray binaries. In this work, we present radio (Arcminute Microkelvin Imager Large Array, MeerKAT), X-ray (*Swift*), and optical (Las Cumbres Observatory) observations of MAXI J1820+070 throughout its entire outburst, including its initial hard state, subsequent soft state, and further hard-state-only re-brightenings (covering March 2018 to August 2022). Due to the regularity and temporal density of our observational data we are able to create a Radio–X-ray–Optical activity plane where we find a high degree of correlation between the three wave bands during the hard states, and observe hysteresis as MAXI J1820+070 enters and exits the soft state. Based on the morphology of the optical light curves we see evidence for optical jet contributions during the soft-to-hard state transition, as well as fading optical emission well before the hard to soft transition. We establish that the remarkably similar profiles of the re-brightening events are broadly consistent with modified disc instability models where irradiation from the inner accretion disc is included.

Key words: stars: black holes – radio continuum: transients – X-rays: binaries.

1 INTRODUCTION

Black hole X-ray binaries (BHXRBs), systems containing a stellar-mass black hole accreting material via an accretion disc from a main-sequence companion, undergo outbursts during which they cycle through characteristic accretion states (e.g. Fender, Belloni & Gallo 2004; Remillard & McClintock 2006). These accretion states are defined predominantly via X-ray observations, particularly the X-ray hardness ratio and timing properties of a system. The *hard* state is characterized by an X-ray spectrum peaking at ∼100 keV with a strong power-law component, and high levels of X-ray variability (Homan & Belloni 2005). In the *soft* state the power-law spectral component disappears or is significantly suppressed and the spectrum is dominated by a multicomponent blackbody peaking at ∼1 keV, as expected from a multitemperature accretion disc, and the X-ray variability is significantly suppressed (e.g. Belloni 2010). During transitions between the hard and soft states BHXRBs are said to be in an intermediate state. Strongly coupled to the accretion state of a BHXRB are its jet properties, observed primarily at radio and (sub-)mm frequencies (e.g. Fender et al. 2004; Russell et al. 2014, 2020; Tetarenko et al. 2019, 2021). In the hard state sources emit flat

★ E-mail: joe.bright@physics.ox.ac.uk

spectrum synchrotron radio emission, consistent with a constantly replenished and collimated outflow (e.g. Blandford & Königl 1979; Falcke & Biermann 1995). The presence of this so-called core jet has been directly confirmed through high resolution radio imaging of GRS 1915+105 (Dhawan, Mirabel & Rodríguez 2000), Cygnus X-1 (Stirling et al. 2001), and most recently and spectacularly in *Swift* J1727.8−1613 (Wood et al. 2024). In the soft accretion state, emission from this core jet is significantly suppressed, or switches off completely, with the current best constraint on the quenching factors on the order of 3 dex (Bright et al. 2020; Maccarone et al. 2020; Russell et al. 2020).

Most BHXRBs spend the majority of their lifetimes accreting at an extremely low rate (e.g. Gallo, Fender & Hynes 2005; Plotkin, Gallo & Jonker 2013; Plotkin et al. 2021; Carotenuto, Corbel & Tzioumis 2022) in a quiescent state (with an unionized disc) or a very dim hard state (Gallo et al. 2005), with their accretion disc (at optical and X-ray wavelengths) and jets (radio wavelengths) frequently undetectable with current observational facilities. Occasionally, likely due to instabilities in the disc, the accretion rate can increase by many orders of magnitude (∼8 dex in the most extreme cases; Rodriguez et al. 2020) resulting in detectable optical and X-ray emission from the (outer and inner) disc, and the presence of compact core jets detectable in radio. A source undergoing such an instability is said to be in outburst. While some sources fade to quiescence after spending time in the hard-state-only (e.g. Tetarenko et al. 2016; Williams et al. 2020; Alabarta et al. 2021), other sources make one or many hard to soft state transitions before returning to the hard state and fading to quiescence (e.g. Fender et al. 1999a; Corbel et al. 2001; Bright et al. 2020; Carotenuto et al. 2021a). Associated with the hard to soft state transition (but not the reverse one) is the launch of bipolar ejections which can travel to large angular separations from the site of the black hole (when compared to the observed head of the core jet), appear no longer physically connected to the black hole, and are resolved from the core position at both radio (e.g. Mirabel & Rodríguez 1994; Fender et al. 1999a; Bright et al. 2020; Wood et al. 2021; Carotenuto et al. 2021a; Bahramian et al. 2023) and X-ray (Corbel et al. 2002; Migliori et al. 2017; Espinasse et al. 2020) frequencies.

The BHXRB MAXI J1820+070 (hereafter J1820) has been the target of intense monitoring campaigns across the electromagnetic spectrum since it began its first known outburst in March 2018, with its brightness allowing observers to collect a wealth of high-quality data from the source and progress our understanding of accretion and jet launching in BHXRBs (e.g. Shidatsu et al. 2019; Bright et al. 2020; Shaw et al. 2021; Echiburú-Trujillo et al. 2024). J1820 was discovered as an optical transient by the All-Sky Automated Survey for SuperNovae (ASAS-SN; Shappee et al. 2014; Kochanek et al. 2017) on 2018 March 06 and labelled ASASSN-18ey (Tucker et al. 2018). Initially classified as a cataclysmic variable (due to its apparent association with a *Gaia* source), J1820 was then detected by the Monitor of All-sky X-ray Image (MAXI; Matsuoka et al. 2009) Gas Slit Camera (Mihara et al. 2011; Sugizaki et al. 2011), assigned the name MAXI J1820, and associated with ASASSN-18ey on 2018 March 11 (Denisenko 2018; Kawamuro et al. 2018) where initial observational evidence suggested it was a BHXRB (Baglio, Russell & Lewis 2018). J1820 initially underwent a 'classical' outburst, with a single hard to soft state transition, followed by a return to the hard state. Instead of immediately returning to quiescence J1820 then underwent three hard-state-only rebrightenings reaching 1 to 10 per cent of the peak luminosity of the initial outburst depending on observing band. The intensive monitoring of J1820 has lead to a number of exciting results. These include an accurately measured radio parallax distance of 2.96 ± 0.33 kpc and position RA $= 18^{\rm h}20^{\rm m}21\overset{\rm s}{.}938$, Dec. $= 07^{\circ}11'07\overset{''}{.}165$ (along with a well constrained proper motion; Atri et al. 2020), the detection of large-scale jet ejections during the hard to soft state transition and strong constraints on their energetics (Bright et al. 2020; Espinasse et al. 2020; Wood et al. 2021), an association between the launch of these transient ejecta and the properties of the accretion flow (Homan et al. 2020; Ma et al. 2021, 2023; Wang et al. 2021; You et al. 2021), measured changes in the geometry of the corona (Kara et al. 2019; Ma et al. 2023), a dynamical confirmation that J1820 harbours a black hole with a low-mass companion (Torres et al. 2019, 2020), and the ability to track the spectral break of the hard state jet over three decades in frequency (Echiburú-Trujillo et al. 2024), to name but a few.

BHXRBs are ideal systems for probing the connection between accretion and the production of jets owing to their rapid evolutionary time-scales during outburst. While it is common to correlate X-ray observations of BHXRBs, which probe the inner accretion disc, with radio observations, which probe the core jet, optical observations are considered in tandem less often (although see e.g. Russell et al. 2006). The origin of the optical emission in BHXRBs is more ambiguous than that of the radio and X-rays, with direct accretion disc photons (Shakura & Sunyaev 1973), reprocessed accretion disc photons (e.g. Cunningham 1976; Vrtilek et al. 1990), and jet photons (e.g. Corbel & Fender 2002; Chaty et al. 2003; Homan et al. 2005), or some combination of the three, all possible contributing sources (see e.g. Russell et al. 2006; Veledina, Poutanen & Vurm 2013; Vincentelli et al. 2021; Saikia et al. 2022, 2023a; Koljonen et al. 2023 for additional interpretations). Additionally, the contribution of the companion star will dominate in the optical and infrared, although this is more prominent for XRBs harbouring a high-mass companion (and less so at the peak of outburst compared to quiescence). Due to this ambiguity, only when high-quality multiwavelength data exist, as is the case for J1820, can we attempt to disentangle these optical emission mechanisms and put them in context with the more frequently produced radio–X-ray correlation. Such observations provide insight into the emission profile and evolution of jets, how their formation is coupled to the inner accretion disc, and how different regions of the accretion disc interact.

In this paper, we present observations of J1820 at radio, optical, and X-ray frequencies between MJD 58 189 (2018 March 12) and MJD 59 792 (2022 August 01). In Section 2, we describe our observations of J1820 and relevant data reduction techniques, in Section 3, we present our radio, optical, and X-ray light curves and correlations between them, and in Sections 4 and 5, we discuss the light curves and correlations in the context of BHXRB accretion models.

2 OBSERVATIONS

2.1 Radio

2.1.1 Arcminute Microkelvin Imager Large Array

Observations of MAXI J1820 with the Arcminute Microkelvin Imager Large Array (AMI-LA; Zwart et al. 2008; Hickish et al. 2018) were triggered automatically in response to a SWIFT Burst Alert Telescope VOEvent (trigger ID 813771) on 2018 March 12 (Staley et al. 2013; Kennea et al. 2018). Manual observations were regularly scheduled thereafter, and remain ongoing. Data were recorded at a central frequency of 15.5 GHz and across a 5 GHz bandwidth consisting of 4096 frequency channels, which we average to eight channels before processing. The AMI-LA data, which measures Stokes $I + Q$, were reduced using a custom pipeline, `reduce_dc`, which flags data for instrumental issues, antenna shadowing, the

effects of weather conditions, and settling times. The software then applies bandpass, absolute flux scale (using either 3C48 or 3C286), and time dependent phase correction (see e.g. Davies et al. 2009; Perrott et al. 2013). The compact source J1824+1044 was used as the phase reference calibrator for all but the first (automatically triggered) observation, which used J1819+0640. We then perform additional flagging using the COMMON ASTRONOMY SOFTWARE APPLICATIONS (CASA 6.4.1.12; McMullin et al. 2007; CASA Team 2022) package, using the `rflag` and `tfcrop` flagging modes. Imaging is performed with the `tclean` task, where we use a Briggs (Briggs 1995) robust weighting of 0.5, which we find to be a good compromise between sensitivity and dirty beam quality, and two Taylor terms to account for the high fractional bandwidth when cleaning. The cell size was fixed to 5 arcsec and we produced 512×512 pixel^2 images which cover the primary beam of the AMI-LA while appropriately sampling the synthesized beam which has typical major and minor axis of 30 and 60 arcsec, respectively (assuming a Gaussian beam). To measure the flux density in each observation we use the CASA task `imfit`, forcing the Gaussian source component to have the same shape as the synthesized beam of the particular observation. Due to the brightness of MAXI J1820 in its initial outburst, as well as the rebrightenings, we are able to measure the amplitudes directly from the complex visibilities, and observe the short time-scale (minutes) variability of J1820, which revealed a flare during the initial hard to soft state transition (Bright et al. 2020). No other such short-term variability is seen during our observations with the AMI-LA. The initial automatically triggered observation was calibrated and imaged manually and the peak pixel was taken as the flux density, with a conservative error of 20 per cent.

In this work, we began with a total of 396 distinct observations of J1820 (defined as individually scheduled observations in the AMI-LA control system, including the initial automatically triggered observation). This large number of observations motivated the automated reduction and imaging procedure described above, however we perform a number of quality cuts on our data before presenting the final light curve of J1820 from the AMI-LA. First, using the CASA task `imfit`, we create a light curve of the phase reference calibrator by fitting a point source component to J1824+1044 in the image plane and rejecting observations (both the calibrator and J1820) for which either the fit did not converge or the ratio of the major to minor full width at half-maximum of the synthesized beam was greater than 10 (which indicates antenna dropout). This cut resulted in the rejection of 11 observations. Phase reference calibrators should be point like and non-variable on the time-scale of an observation length. Longer term variability in the flux density of a phase reference calibrator is acceptable, but apparently large short time-scale variability could also indicate poor calibration of the flux density scale for a given observation. As such, we calculate the average value of the flux density measured from the phase reference calibrator and reject observations (both the calibrator and J1820) where we measure the flux density of the phase calibrator to be discrepant from the average by more than 15 per cent, which resulted in a further 24 observations being rejected. The light curve of J1824+1044 is shown in Fig. 1 and demonstrates a number of flux density measurements significantly different from the average, which would imply large flux density changes on short (day length) time-scales. This process filtered out obvious outliers in the light curve of J1820. After removing these 35 observations the calibrator is variable at the ∼5 per cent level whereas before filtering out the 24 unreliable measurements the variability was ∼10 per cent. Based on this we assign a 5 per cent uncertainty to our flux measurements of J1820 added in quadrature to the statistical uncertainty derived from the image plane fitting.

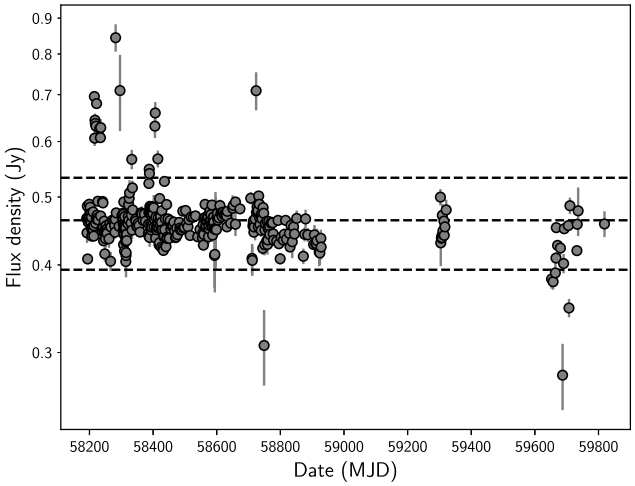

Figure 1. The light curve of the phase reference calibrator J1824+1044. Errors on data points indicate the statistical uncertainty from the `imfit` task. The central dashed line marks the mean flux density of J1824+1044 and the lines above and below it mark 1.15 times the mean flux density and 0.85 times the mean flux density, respectively. We reject observations of J1820 for which the flux density of J1824+1044 is outside of this range as they indicate a poor transfer of the flux density scale for that observation.

Table 1. Arcminute Microkelvin Imager Large Array observations of MAXI J1820. A full machine readable table is available as part of the online version of this article. Errors are statistical only, and should be combined in quadrature with a 5 per cent calibration uncertainty. Note that the first observation was triggered automatically in response to a *Swift*-BAT VOEvent trigger.

Date (dd/mm/yy)	MJD mid-point	Flux density (mJy)
12/03/18	58189.1121	2.49 ± 0.50
14/03/18	58191.2914	17.13 ± 0.16
15/03/18	58192.2887	21.59 ± 0.45
16/03/18	58193.2860	31.69 ± 0.25
18/03/18	58195.2805	50.78 ± 0.27
...	...	...

Finally, we manually inspected all images of J1820 for which the flux density was below 500 μJy, resulting in the rejection of 34 additional observations. Observations for which the fitted flux density was less than five times the image RMS noise were labelled as upper limits. After these cuts, we are left with 326 distinct observations (including upper limits). We include a sample of our AMI-LA observations in Table 1 and a machine readable table covering our entire observing campaign is available as part of the online version of this article.

2.1.2 MeerKAT

As part of the ThunderKAT large survey project (Fender et al. 2016) we began observing the field of MAXI J1820 with the MeerKAT telescope on 2018 September 28 when the source appeared clearly extended (with angular extents ∼10 arcsec) due to the presence of large-scale ejections launched during the hard to soft state transition (Bright et al. 2020), with a typical MeerKAT resolving beam being ∼7 arcsec. Note that this does not violate our assumption of a point source for our AMI-LA observations as during the soft state the transient ejecta were significantly closer to the core, and are

Table 2. Meerkat observations of MAXI J1820. Errors are statistical only and as such a 5 per cent calibration error should be added in quadrature when using these data. A full machine readable table is available as part of the online version of this article. The 'Obs. ID' column can be used to identify observing blocks in the MeerKAT data archive (https://apps.sarao.ac.za/katpaws/archive-search).

Obs. ID	Date (dd/mm/yy)	MJD mid-point	Flux density (mJy)	Image RMS (μJy beam^{-1})
1538156623	28/09/18	58389.75	3.47 ± 0.05	41
1538757039	05/10/18	58396.70	11.8 ± 0.1	72
1539354654	12/10/18	58403.66	2.62 ± 0.04	37
1539529257	14/10/18	58405.67	2.41 ± 0.03	24
1539955889	19/10/18	58410.62	1.52 ± 0.06	50
...	...	...	...	...

sub-dominant at 15.5 GHz once the hard state core jet reignites. We continued observing J1820 with MeerKAT until August 2022. MeerKAT data were reduced using the `oxkat` data reduction pipeline (Offringa et al. 2014; Kenyon et al. 2018; Makhathini 2018; Heywood 2020; Hugo et al. 2022) which performs phase reference calibration as well as phase and amplitude self-calibration (we do not employ direction dependent calibration techniques, although `oxkat` includes that capability, due to the relative simplicity of the sky brightness distribution in the region surrounding MAXI J1820). We used the flux standard J1939−6342 to calibrate the absolute flux density scale and bandpass response of the instrument, while J1733−1304 was used to calibrate the time-dependent complex gains. We used a Briggs robust weighting of −0.3 when imaging (Briggs 1995).

For observations taken on and before MJD 58 454 core flux densities are taken from Bright et al. (2020), where multiple point source components were used to describe the flux of the core and approaching and receding transient ejecta. The same data reduction procedure was used in Bright et al. (2020) as for this work. For observations between MJD 58 460 and MJD 58 551 there is still low-level emission from the receding ejections component but we are unable to satisfactorily fit multiple emission components to the extended morphology. We fit an unresolved point source to these data as the core is the dominant component but note that the low level emission might distort the fit to a small extent. After MJD 58 511 the emission from J1820 is entirely core dominated, and we fit an unresolved source to a small region around the source position. A 5 per cent calibration uncertainty is added in quadrate to the uncertainty derived from `imfit`. The MeerKAT data detailing the flux density of the core jet from J1820 are (partially) given in Table 2, with a full machine readable table covering our entire observing campaign available as part of the online version of this article.

2.2 X-rays: *Swift*

MAXI J1820 was observed thoroughly by the *Swift* X-ray Telescope (hereafter XRT; Gehrels et al. 2004; Burrows et al. 2005) onboard the *Neil Gehrels Swift Observatory* (*Swift*) beginning on MJD 58 189 (2018 March 12) and ending on MJD 59 735 (2022 June 05). Observations were conducted both in Proportional Counter (PC) mode and Windowed Timing (WT) mode. To produce an X-ray light curve for J1820 we first built spectra for each observation ID (obsID) using the *Swift*-XRT data product generator[1] (Evans et al. 2009). Spectra that contained at least 300 total counts were then binned using `grppha` such that each bin had a minimum of 20 counts. For spectra with less than 300 total counts no binning was performed. To determine the flux associated with each spectrum they were loaded into XSPEC (version: 12.14.0b; Arnaud 1996) where we ignore bad data and ignore data outside of the range 0.5 to 10 keV. We discard spectra for which the time on source was less than 1 min, there were fewer than 15 counts in WT mode, or there were fewer than 3 counts in PC mode. We then proceed to fit the spectra, with the method depending on the total counts. For spectra with less than 300 total counts we use Cash statistics to constrain our fitting and only consider an absorbed power-law model [`tabs(pow)` in XSPEC], with fixed neutral hydrogen column density ($n_{\rm H} = 0.091$), and fixed photon index ($\Gamma = 1.7$) if the total counts were below 50. After identifying the best-fitting model parameters we freeze them and introduce a flux parameter so that the new model is `tabs*cflux(pow)` and `cflux` is the only free parameter. This model is then fit again to constrain `cflux` and its value and 1σ error are extracted. For spectra with 300 or above total counts the procedure is much the same, however during the soft and intermediate states defined in Shidatsu et al. (2019) we compare both a power law and power law plus disc blackbody [`tabs(pow + diskbb)` in XSPEC] model, selecting the favoured model using an F-test with a P value below 0.001 required to accept the more complex model. As in the previous case, we then calculated the final flux through the addition of the `cflux` parameter. Due to the higher counts for these spectra we use the Chi-squared test statistic to determine the quality of the fit. A sample of our X-ray observations are given in Table 3 with a full version available in the online version of this article.

Table 3. *Swift*-XRT observations of MAXI J1820. A full machine readable table is available as part of the online version of this article.

Mode	Date (dd/mm/yy)	MJD mid-point	Flux ($\times 10^{-9}$ erg s^{-1})
WT	12/03/18	58189.0814	1.91 ± 0.01
PC	12/03/18	58189.1217	1.52 ± 0.01
WT	13/03/18	58190.7401	4.19 ± 0.02
WT	14/03/18	58191.8369	6.10 ± 0.01
WT	14/03/18	58191.8786	5.86 ± 0.02
...	...	...	...

2.3 Optical

Comprehensive optical monitoring of MAXI J1820 was performed with telescopes at the Las Cumbres Observatory (LCO). Data were taken during the initial 2018 outburst, and during the multiple rebrightening events (e.g. Baglio et al. 2018, 2021; Russell et al. 2019a; Russell, Baglio & Lewis 2019c), as part of a monitoring campaign of ∼50 low-mass X-ray binaries coordinated with the Faulkes Telescope Project (Lewis et al. 2008; Lewis 2018). The monitoring includes data taken at the 2-m Faulkes Telescopes at Haleakala Observatory (Maui, Hawai'i, USA) and Siding Spring Observatory (Australia), and the 1-m telescopes at Siding Spring Observatory, Cerro Tololo Inter-American Observatory (Chile), the South African Astronomical Observatory (SAAO; South Africa), and the McDonald Observatory (Texas, USA). For the purposes of this

[1] https://www.swift.ac.uk/user_objects/

Table 4. LCO observations of MAXI J1820 taken with the SDSS g' filter. The error reported here includes a 0.04 magnitude error combined in quadrature with the statistical error. A full machine readable table is available as part of the online version of this article.

Date (dd/mm/yy)	MJD mid-point	Apparent magnitude
13/03/18	58190.3864	13.11 ± 0.04
14/03/18	58191.4074	12.93 ± 0.04
14/03/18	58191.7960	12.90 ± 0.04
17/03/18	58194.3964	12.42 ± 0.04
18/03/18	58195.3420	12.43 ± 0.04
...	...	...

Table 5. LCO observations of MAXI J1820 taken with the SDSS i' filter. The error reported here includes a 0.04 magnitude error combined in quadrature with the statistical error. A full machine readable table is available as part of the online version of this article.

Date (dd/mm/yy)	MJD mid-point	Apparent magnitude
13/03/18	58190.3864	13.04 ± 0.04
14/03/18	58191.4074	12.93 ± 0.04
14/03/18	58191.7960	12.84 ± 0.04
17/03/18	58194.3964	12.52 ± 0.04
18/03/18	58195.3420	12.17 ± 0.04
...	...	...

work we make use of the images taken using the SDSS g' and i' filters.

The LCO data were initially processed using the LCO Banzai pipeline (McCully et al. 2018). Reduction and analysis of the reduced images was achieved using the real-time data analysis pipeline, XB-NEWS (the X-ray Binary New Early Warning System; see Russell et al. 2019a; Goodwin et al. 2020; Pirbhoy et al. 2020). The XB-NEWS pipeline downloads images of targets of interest from the LCO archive soon after they are taken by the telescopes, along with their associated calibration data. Then, the pipeline performs quality control steps to ensure that only good quality images are analysed, and produces an astrometric solution for each image using *Gaia* DR2 positions.[2] Aperture photometry was then performed on all the stars in each image, solving for the zero-point calibrations between epochs (Bramich & Freudling 2012). The ATLAS All-Sky Stellar Reference Catalog (ATLAS-REFCAT2; Tonry et al. 2018) was used for flux calibration. The pipeline also performed multi-aperture photometry [azimuthally averaged point spread function (PSF) profile fitting photometry; Stetson 1990] for point sources. We detect the source with high significance throughout the outburst and rebrightenings. We add a systematic 0.04 magnitude error in quadrature with the error reported via the data reduction pipeline. A sample of our optical observations are given in Tables 4 and 5 with a full version available in the online version of this article. We convert our optical magnitudes to luminosities using $L_O = 4\pi d^2 10^{-(m+48.585-yA_v)/2.5}(c/\lambda)$ where m is the apparent optical magnitude, d is the distance to J1820, c is the speed of light, and λ is the central frequency of the filter being used. We have corrected for extinction using $A_v = 0.558$ from Tucker et al. (2018) and filter specific extinction coefficients (y) from Cardelli, Clayton & Mathis (1989). All observational data can also be found in machine readable format at the Zenodo, doi: 10.5281/zenodo.15721448.

[2]https://www.cosmos.esa.int/web/gaia/dr2

3 RESULTS

3.1 Light curves

Fig. 2 shows the radio, X-ray, and optical luminosity of J1820 spanning ∼1600 d since its initial rise out of quiescence. Combinations of the radio, X-ray, and optical observations of the initial hard state, subsequent soft state and the following hard state have been analysed to an extent in other works (e.g. Shidatsu et al. 2019; Shaw et al. 2021; Tetarenko et al. 2021; Echiburú-Trujillo et al. 2024) but have not been presented together and with such comprehensive coverage as in Fig. 2.

In addition to the initial 'canonical' outburst, we show data from three hard-state-only (evidenced by the radio spectral index also shown in Fig. 2) rebrightenings, which we label R1, R2, and R3, in chronological order. These rebrightenings are obvious at radio, X-ray, and optical wavelengths, and show remarkably similar light curve morphologies with a fast rise and a decay characterized by two distinct decay rates, an initially shallow decay followed by a faster decline most easily seen in the AMI-LA 15.5 GHz radio data (see also Fig. 8 for isolated light curves of the rebrightenings). As expected for hard-state-only outbursts we see no evidence for the launch of transient ejecta in our MeerKAT images during any of the three rebrightenings, although MeerKAT only probes structures down to a size scale of a few seconds of arc. Additionally, it is worth noting the similarity of the hard state immediately following the soft to hard state transition (sometimes called the fading hard state, which we label R0) with the subsequent rebrightenings, minus the initial flare as the core jet reignites. We discuss these similarities in Section 4.1.

After around MJD 59 000 J1820 ceased entering into hard-state-only rebrightenings. The lack of regular sampling after this date (partly due to the Coronavirus pandemic in 2019) does not indicate that rebrightening events were missed, as MAXI would have detected such events and AMI-LA/MeerKAT/*Swift* observations would have been triggered in response. Dense optical monitoring was undertaken between MJD ∼ 59000 and MJD ∼ 59800 and showed no rebrightening events in this time. The source was clearly still detected, and appeared to steadily rise in luminosity in both of our optical observing bands significantly above the Panoramic Survey Telescope and Rapid Response System (PanSTARRS) archival limits from the system. True quiescence was only reached as recently as June 2023 (MJD 60106) well beyond the coverage of the observations presented here (see Baglio et al. 2023) indicating a low level of activity after the re-brightening events ended.

3.2 Correlations

Due to our dense temporal sampling of J1820 at radio, X-ray, and optical wavelengths we are able to construct various two way correlations, as well as a radio–X-ray–optical activity plane, for the entire outburst. We are also able to produce a correlation for the canonical outburst and re-brightening events separately to check for any differences in behaviour. In all following cases, we correlate the data by taking the two (or three) light curves being correlated and dividing the time range covered into bin sizes of 1.5 d (1.8 d for the radio–X-ray–optical correlation). These time-scales were selected to maximize the number of data points for correlation, without correlating data on time-scales longer than those typically seen in

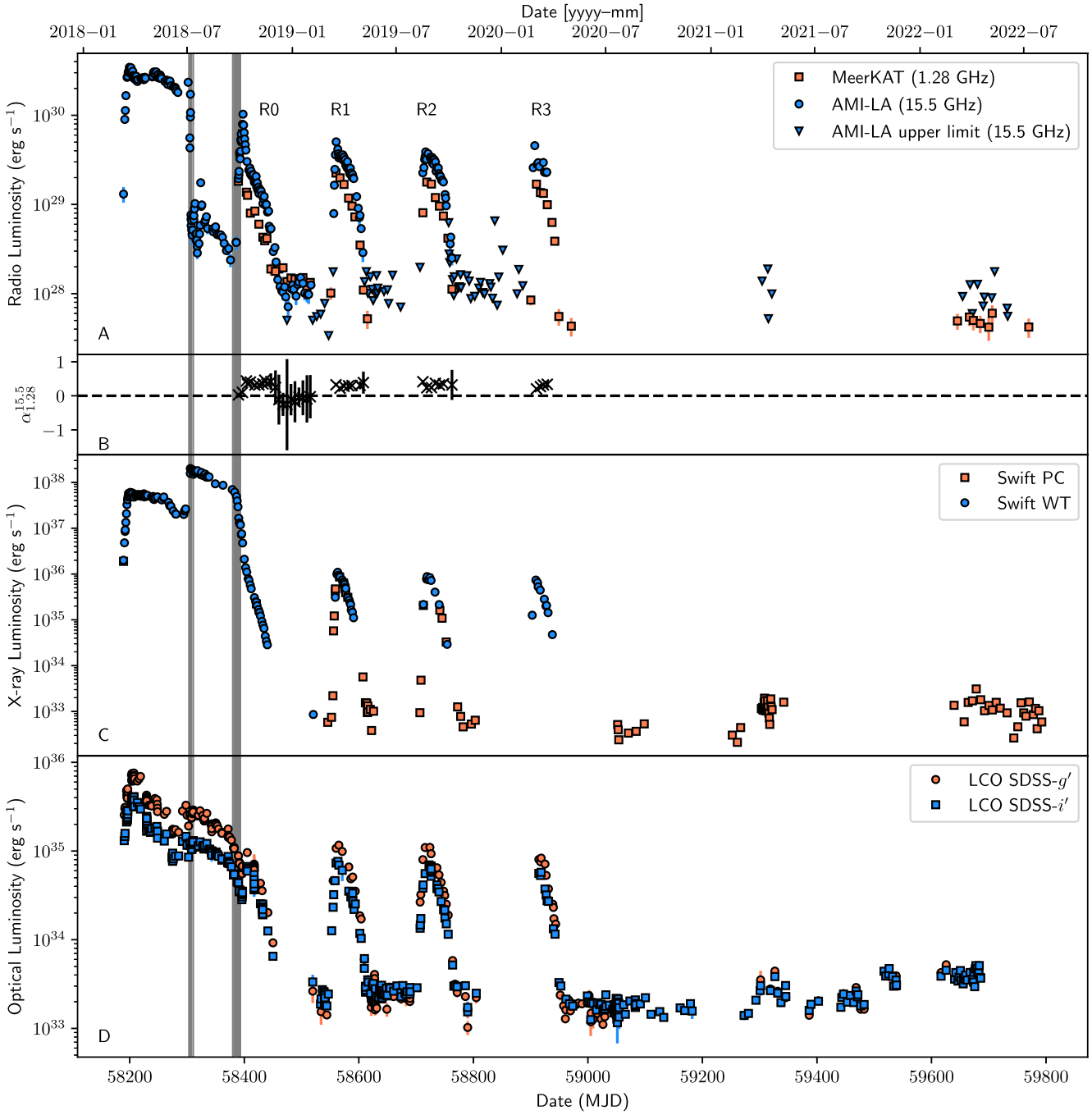

Figure 2. Radio (Arcminute Microkelvin Imager Large Array, MeerKAT), X-ray (*Swift*), and optical (Las Cumbres Observatory) light curves of MAXI J1820. A distance of 2.96 kpc was assumed for the conversion to luminosity (Atri et al. 2020). Grey shaded regions mark times during which J1820 was in the intermediate state according to Shidatsu et al. (2019). **Panel A:** MeerKAT 1.28 GHz and AMI-LA 15.5 GHz radio observations of J1820+070. See the main text for how flux densities and upper limits were derived. AMI-LA upper limits are 5σ. Note that we assume a flat spectrum and scale to a common frequency of 5 GHz when converting from flux density to luminosity. **Panel B:** the Radio spectral index between 1.28 and 15.5 GHz with the convention $F_\nu(\nu) \propto \nu^\alpha$. The horizontal dashed black line corresponds to a flat radio spectrum ($\alpha = 0$). The spectral index was calculated for each MeerKAT point using the nearest in time AMI-LA observation, if an observations existed within 2 d of the MeerKAT one. **Panel C:** *Swift* X-ray Telescope 0.5–10 keV luminosity of J1820 taken both in windowed timing and proportional counter mode. **Panel D:** optical g' and i' luminosity of J1820 taken from the Las Cumbres Observatory. The central frequency of the g' and i' filters were used to convert to a luminosity.

X-ray binary evolution. Within each bin we check for observations taken at the wavelengths being correlated. If none are found, that bin is ignored. If a single measurement from each wavelength is found then this is used in the correlation. If multiple measurements are found within a bin then their average is used, with the error on the average taken to be the standard deviation of the measurements within the bin. Upper limits are not considered in any of our correlations.

When fitting two way correlations we use the PYTHON SCIPY orthogonal distance regression (ODR) module to fit power law

functions to the correlated data of the form $L_1 = AL_2^a$, where L_1 and L_2 are luminosities at observing bands 1 and 2, respectively, and we refer to a and A as the power-law index and scaling factor, respectively. ODR in SCIPY accounts for errors on both the 'independent' and 'dependent' variables (x and y) as is appropriate when correlating measured data. We fit the logarithm of our data such that the function describing the correlation is linear.

When considering the correlation between radio, optical, and X-ray measurements we fit a line to the logarithmic data using a power iteration algorithm which converges to a line of best fit (defined by the centroid, $[L_{X,0}, L_{R,0}, L_{O,0}]$ and unit direction vector $[a, b, c]$) according to a minimization of the sum of the orthogonal distance in three dimensions. In order to calculate the error on our fitted parameters, we assume that the errors on each point in the three dimensional space is Gaussian and we sample 1000 sets of points and perform the fitting for each set, taking the error on each parameter as the standard deviation of the output from the 1000 fitting runs. We give the correlation parametrically as

$$\begin{bmatrix} L_X \\ L_R \\ L_O \end{bmatrix} = \begin{bmatrix} L_{X,0} \\ L_{R,0} \\ L_{O,0} \end{bmatrix} + t \begin{bmatrix} a \\ b \\ c \end{bmatrix} \tag{1}$$

where t can be used to describe any point on the line.

3.2.1 *Radio–X-ray correlation*

During the hard accretion state the radio emission from BHXRBs, emanating from a compact core jet, is strongly coupled to the X-ray emission. To first-order this radio–X-ray correlation can be separated into two 'tracks', named radio-loud and radio-quiet (or the standard and outlier tracks, respectively; e.g. Gallo, Miller & Fender 2012; Motta, Casella & Fender 2018). The majority of BHXRBs lie on the radio-quiet (outlier) track, showing a deviation from the standard track at high luminosities (showing a steeper correlation of $L_R \propto L_X^{>1}$) and rejoining it when decaying into quiescence (e.g, Coriat et al. 2011; Carotenuto et al. 2021b). J1820 is an example of a radio-loud source, exhibiting an approximate correlation $L_R \propto L_X^{0.6}$ (e.g. Corbel et al. 2000, 2003) that persists over a large range in radio and X-ray luminosities (Tremou et al. 2020; Shaw et al. 2021). During its initial outburst J1820 was shown to follow the radio-loud track with a marginally shallower correlation than expected, with index 0.50 ± 0.09 (Bright et al. 2020). The correlation appeared particularly shallow during the hard state immediately following the soft state associated with the launch of transient ejecta (which we label R0), with an index of 0.37 ± 0.03 in the X-ray luminosity region between $\sim 10^{34}$ and $\sim 10^{36}$ erg s^{-1} as is evident in Fig. 3 (and can be seen more clearly in fig. 1 of Bright et al. 2020). Combining all of our hard state data we derive a global relation of

$$L_R \propto L_X^{0.481\pm0.009} \tag{2}$$

for the AMI-LA data, and a marginally shallower

$$L_R \propto L_X^{0.41\pm0.03} \tag{3}$$

for the MeerKAT data. These are also both consistent with what was derived in Bright et al. (2020) and Shaw et al. (2021), with marginally shallower than the canonical value of ~ 0.6 for radio-loud BHXRBs. To convert our flux densities to luminosities we have used the spectral indices in panel B of Fig. 1. If a radio observation is within 3 d of an epoch where a spectral index is measured, then that spectral index is used to shift the AMI-LA or MeerKAT observation to a flux density at 5 GHz. If no spectral index is found within 3 d then the median spectral index (excluding the time range where the spectral index was negative) was used to scale the data. Soft state, intermediate state, and the data where the spectral index was negative were not scaled. These data are not included in the correlations. This process is used for all correlations involving radio observations, but not for light curves, where a flat spectrum at the central observing frequency is assumed. When fitting the correlation we ignore hard state data within 5 d of the state transition outlined by Shidatsu et al. (2019) motivated by the clear drop in radio emission seen in Fig. 3 before the hard to soft state transition. The points are encircled in Fig. 3.

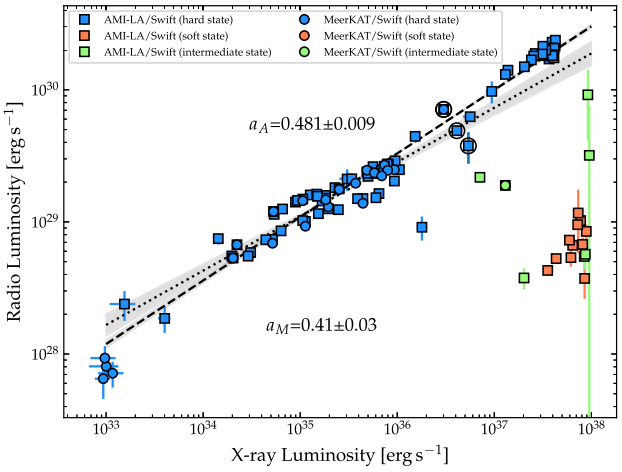

Figure 3. The radio–X-ray correlation for J1820, including data from the initial outburst (as seen in Bright et al. 2020), and the three rebrightening events shown in Fig. 2. Squares show data taken with the AMI-LA recorded at 15.5 GHz and circles show data from MeerKAT recorded at 1.28 GHz. Blue, green, and orange indicate the spectral state of the source when the data were recorded, showing hard, intermediate, and soft, respectively. The two annotated dashed lines show best power-law fit to the data from the AMI-LA (top line) and MeerKAT (bottom line) with the error region shaded in grey. Soft state data are not included in the fit as it can be attributed to emission from transient ejecta launched during the hard to soft state transition (Bright et al. 2020). The data have been scaled to a common luminosity at 5 GHz assuming a spectral index as defined in Section 3.2.1. Hard state observations within 5 d of the state transitions outlined in Shidatsu et al. (2019) are encircled.

To check for different behaviour during the three re-brightening events we show the radio X-ray correlation for data post MJD 58 500 in Fig. 4. The slope during the re-brightenings is best measured by the AMI-LA (squares) and shows an apparent flattening from $L_R \propto L_X^{0.481\pm0.009}$ to $L_R \propto L_X^{0.37\pm0.02}$. It is interesting to note that this is the same X-ray luminosity range that showed a flatter correlation in Bright et al. (2020), which just considered R0. The slope derived from the MeerKAT data is consistent with the full correlation with $L_R \propto L_X^{0.41\pm0.04}$.

3.2.2 *Optical–X-ray correlation*

The optical–X-ray correlation is shown for g'- and i'-band data in Fig. 5. During the majority of the hard state there is a clear correlation between optical and X-ray frequencies, however there are clear deviations from the general correlation at low and high luminosities. Indeed, it is clear from Fig. 2 that during the initial hard state (also known as the rising hard state, before ∼MJD 58300), after the first peak, the optical emission was dropping while the X-rays and radio stayed relatively constant (and correlated, see Fig. 3) before dipping slightly then rising as the X-ray spectrum softens and the hard to soft state transition occurred (the optical fade and

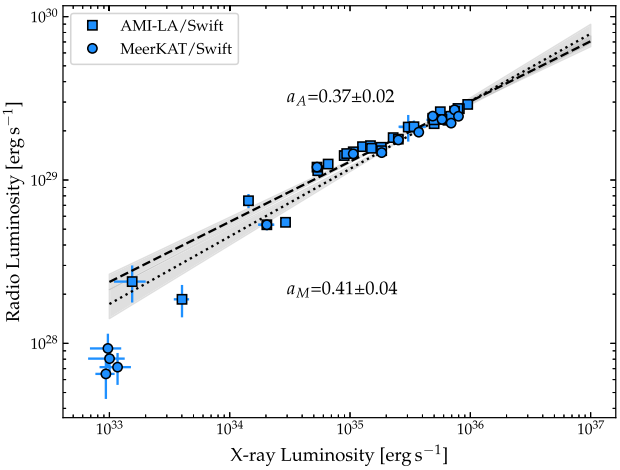

Figure 4. As for Fig. 3 but only including data post MJD 58 500 which includes the hard-state-only rebrightenings only. Due to our lack of early MeerKAT coverage the fit for those data is similar to the one in Fig. 3 at $a_M = 0.41 \pm 0.04$, whereas the AMI-LA correlation is significantly shallower with $a_A = 0.37 \pm 0.02$.

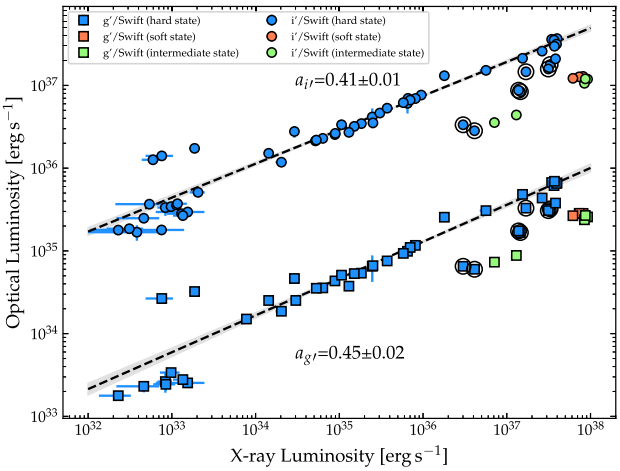

Figure 5. The i'-band (top; multiplied by 10^2 for clarity) and g'-band (bottom) optical–X-ray correlation for J1820. Blue, green, and orange points are the hard, intermediate, and soft states, respectively. For the hard state we distinguish points before MJD 58233.5 by circling them and ignoring them when fitting the hard state correlation as they clearly do not follow the X-ray emission as seen for the rest of the hard state, falling significantly below the correlation at the end of the rising hard state. The black dashed lines shows a power-law fit to the blue data (minus those circled) with indices $a = 0.45 \pm 0.02$ and $a = 0.41 \pm 0.01$ for g' and i' band, respectively.

dip, and the dependence of the optical–X-ray correlation with X-ray energy, are investigated in Yang et al. 2025). We circle these points in the optical–X-ray correlation in Fig. 5 and do not include them when fitting a power law to the relationship, which we find to be $L_{g'} \propto L_{\rm X}^{0.45\pm0.02}$ and $L_{i'} \propto L_{\rm X}^{0.41\pm0.01}$ in the hard state. These are similar to the optical–X-ray correlation slopes of J1820 measured in the soft state, $L_O \propto L_X^{0.51\pm0.03}$, by Shidatsu et al. (2019), but significantly shallower than the (population based) $L_{\rm OIR} \propto L_{\rm X}^{0.61\pm0.03}$ measured in (Russell et al. 2006) (although the correlation was constructed using optical/near-IR bands B to K). It is also clear that the correlation has more scatter at low luminosities, at around

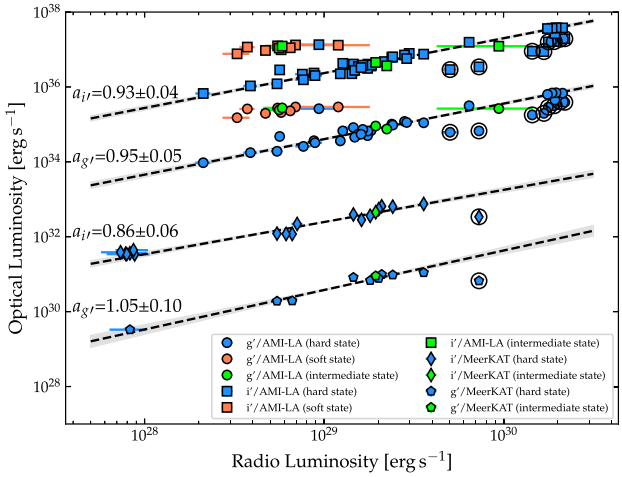

Figure 6. The radio–optical correlation for J1820 using data from MeerKAT, AMI-LA, and the g and i filters from LCO. The power law index of the fit for each pair is given next to the corresponding line. Blue, green, and orange points are the hard, intermediate, and soft states, respectively. From top to bottom the correlations shows optical i' with AMI-LA (squares), optical g' with AMI-LA (circles), optical i' with MeerKAT (diamonds), and optical g' with MeerKAT (pentagons). The optical luminosities have been offset to allow multiple correlations to be displayed on the same figure. For the hard state we distinguish points before MJD 58233.5 by circling them and ignoring them when fitting the hard state correlation. Data have been offset by 10^2, 10^0, 10^{-2}, and 10^{-4} from top to bottom for clarity.

10^{33} erg s^{-1} in X-ray luminosity, where the optical is overpredicted, but also with a few optical points brighter than the extrapolated correlation. These high luminosity optical points correspond to the soft to hard state transition and are discussed in detail later Section 4.1.

3.2.3 *Radio–optical correlation*

Similar to the radio–X-ray and optical–X-ray correlations there is evidently strong coupling between radio and optical wavelengths. Fig. 6 demonstrates these correlations using both of our optical bands and radio data at 1.28 GHz and 15.5 GHz from MeerKAT and the AMI-LA, respectively. As seen for the optical–X-ray correlation a drop in the optical without response from the radio emission is evident during the rising hard state, followed by a rapid drop in the radio during the hard to soft state transition with a marginal re-brightening in the optical (most clear when correlating with the AMI-LA data due to the higher temporal density of the sampling). As before, we ignore data before MJD 58233.5 when fitting the correlations, which we find to be $L_{i'} \propto L_{\rm R}^{0.93\pm0.04}$, $L_{g'} \propto L_{\rm R}^{0.95\pm0.05}$, $L_{i'} \propto L_{\rm R}^{0.86\pm0.06}$, and $L_{g'} \propto L_{\rm R}^{1.1\pm0.1}$ from top to bottom in Fig. 6. The top two correlations are made with AMI-LA data and the bottom two with MeerKAT data. The measured correlation indices are broadly consistent, with the two MeerKAT–optical correlations less well-constrained than those from the AMI-LA. During the intermediate state the radio quenches significantly with little response in the optical.

We show the fitting results of all two-dimensional correlations in Table 6, including the correlation index, scaling factor, and the reduced χ-square statistic for each fit. The reduced χ-squared values for all of our fits are significantly larger than 1, indicating residual scatter not being described by the model. This is likely caused by

Table 6. Power-law fitting parameters between our radio, X-ray, and optical data when J1820 was in the hard accretion state. Data are fit according to $L_1 = AL_2^a$ (for $L_1 - L_2$ in the table below), where a is the power-law index and A is the scaling factor. The reduced χ-squared statistic (χ-squared per degree of freedom) χ_ν is given in the final column which describes the quality of the fit.

Correlation	Power-law index (a)	Scaling factor (A)	χ_ν
1.28 GHz–X-ray	0.41 ± 0.03	15 ± 1	9.4
15.5 GHz–X-ray	0.481 ± 0.009	12.2 ± 0.3	11.3
g' band–1.28 GHz	1.1 ± 0.1	4 ± 3	3.9
i' band–1.28 GHz	0.86 ± 0.06	9 ± 2	4.2
g' band–15.5 GHz	0.95 ± 0.05	7 ± 1	6.8
i' band–15.5 GHz	0.93 ± 0.04	7 ± 1	4.5
g' band–X-ray	0.45 ± 0.02	19.1 ± 0.7	12.4
i' band–X-ray	0.41 ± 0.01	20.1 ± 0.5	7.7

our data not being strictly simultaneous, some uncorrelated optical–X-ray behaviour in the system, or short term optical variability (e.g. Paice et al. 2019).

3.2.4 Radio–X-ray–optical correlation

We show a projection of the three dimensional radio–X-ray–optical activity space of J1820 throughout its outburst in Fig. 7. Unsurprisingly, during the hard state, the three wavebands are strongly correlated and lay along a line with centroid $[L_{X,0}, L_{R,0}, L_{O,0}] = [35.984 \pm 0.003, 29.510 \pm 0.006, 35.105 \pm 0.008]$ and unit direction vector $[a, b, c] = [0.846 \pm 0.002, 0.383 \pm 0.003, 0.371 \pm 0.005]$, with parameters defined in Section 3.2. The dropping optical emission in the rising hard state can be seen in the cluster of blue points at highest optical luminosity, and a hysteresis pattern through the hard–soft–hard transition series is evident. Due to the requirement of having three data points within a time bin we have fewer points in the three dimensional correlation when compared to the two-dimensional ones.

4 DISCUSSION

4.1 Light curve morphologies

The radio, X-ray, and optical light curves of J1820 (Fig. 2) represent a complete look at the entirety of a canonical BHXRB outburst and multiple hard-state-only re-brightening events. There are a number of striking features that we highlight here (and which will be discussed in more detail in the following sections). The most obvious is the high degree of correlation in the three observing bands. During both hard states in the canonical outburst (the rising hard state and R0) the three bands evolve in a similar way, with the exception of the significant jet quenching in the soft state indicated by the sharp drop in radio flux density (with the low level emission caused by transient ejecta; see Bright et al. 2020; Espinasse et al. 2020; Wood et al. 2021) and the early fading optical in the rising hard state. The similarity of the multiwavelength data during the three re-brightening events is particularly notable (see Fig. 8), with the same sharp rise to maximum, and changing decay rate during the decay, visible in all bands. The peak of the three rebrightenings is also relatively stable, as is their spacing. There is also an obvious similarity with the fading hard state (R0; which becomes optically thin around MJD 58460, likely due to the ejecta becoming dominant) and the rebrightening events (R1, R2, R3) not seen in the rising hard state. Optical observations during the periods between rebrightenings show a persistent level of emission also seen at X-ray and radio wavelengths, indicating that the source did not reach quiescence between rebrightenings (Baglio et al. 2023). The optical, X-ray, and radio observations made after MJD $\sim$ 59000 indicate that J1820 has entered a relatively stable phase with a slowly rising optical (and possibly X-ray) luminosity. While our radio and X-ray coverage was less complete in this phase it is unlikely that we missed any similar re-brightening events, given that they would have been detectable by our comparatively more regular optical monitoring since R3. Note that optical observations taken in June 2023 (MJD 60106; later than the observations presented in Fig. 2) suggest that the optical emission from J1820 finally reached its pre-outburst level after 5 yr of activity (Baglio et al. 2023).

We note the sharp rise in optical luminosity after the return to the hard state at MJD $\sim$ 58400 while the radio emission rises rapidly and the X-ray emission is declining (see Fig. 10). If the optical emission we see is entirely associated with reprocessed X-ray emission from the inner accretion disc then we would expect the optical emission to follow it tightly. This opposite behaviour is suggestive of a potential jet contribution to the optical, with the radio and optical emission now coupled instead. This jet contribution to the optical emission has been confirmed by broadband spectral modelling (Özbey Arabacı et al. 2022; Echiburú-Trujillo et al. 2024) and optical polarization evolution during state transitions (Veledina et al. 2019).

The rebrightening events R1, R2, and R3 show remarkable similarities in their light curve morphologies as seen from both MeerKAT and the AMI-LA (Figs 8 and 9 show the radio rebrightenings). It is also notable that the rebrightening events are relatively regularly spaced and reach a similar peak flux density for each flare. The hard state at the end of the canonical outburst (R0) also shows similarity to the rebrightening events with the exception of a higher peak flux density. The hard state immediately preceding the soft state shows no such similarity, demonstrating a relatively constant flux for around 100 d after the start of the outburst. The regularity of the rebrightenings (both temporally and in morphology) suggests that their evolution is being regulated by a common process. The peak X-ray luminosity of the rebrightenings, $\sim 10^{36}$ erg s^{-1}, corresponds to ~ 0.2 per cent of the Eddington limit for a black hole mass of 8.5 $M_\odot$ (Muñoz-Darias et al. 2019) and the total flare time-scale is around 50 to 60 d. The spectral index evolution throughout each rebrightening is also similar, showing a flat or slightly inverted radio spectrum for the duration. There are also two clear decay rates during the fading, with a shallow decay for around 30 d followed by a steeper decay for around 20 d until radio emission is no longer detected. This is most clearly seen in the AMI-LA radio and optical light curves due to their higher time density sampling.

Saikia et al. (2023b) compiled a list of LMXBs with re-brightening events within 1 yr of the end of the initial outburst. Similarities are clear between J1820 and the optical observations of *Swift* J1910.2−0546 (J1910.2) which showed optical reflaring on a $\sim$ 45 d time-scale, although with less well-sampled light curves than for J1820. The flaring in J1910.2 also peaked at an approximately consistent luminosity, similar to J1820, although the spacing between flares was significantly shorter, and the flare profile different. The lack of comprehensive X-ray and radio observations prevents comparison at these wavelengths. Reflaring events have also been observed in MAXI J1535−571 (J1535; Parikh et al. 2019; Cúneo et al. 2020), however in this case the flare amplitude decreased with each subsequent flare and the profile was markedly smoother and more symmetric than for J1820. Additionally J1535 was undergoing state transitions (seen in the hardness intensity diagram and through

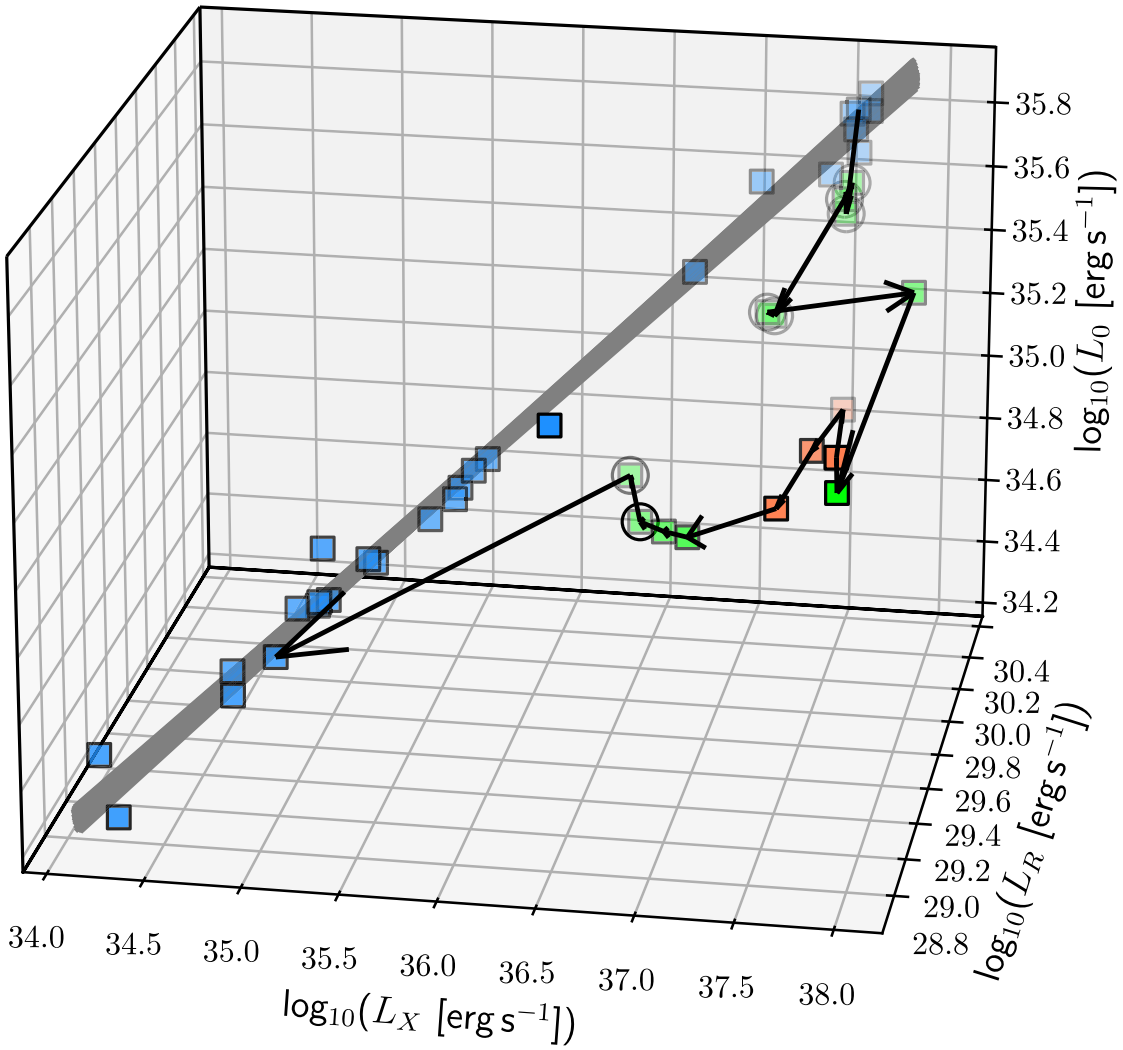

Figure 7. The radio–X-ray–optical correlation plane for J1820. Blue, green, and orange points indicate that the source was in the hard, intermediate and soft states, respectively. The grey shaded region indicates the best-fitting line to the hard state data from all three wavelengths with the thickness of the region showing the 1σ error on the fit. Errors on data points are not shown on this plot. The black solid arrows connect points chronologically from the final point during the rising hard state, through the intermediate and soft states, and back to the first point of the fading hard state to guide the eye. The transparency of point indicates their depth in the three dimensional space, with fainter points at a greater depth. See https://joesbright.github.io/MAXIJ180 for a fully interactive version of this figure.

jet quenching) which J1820 was certainly not (Parikh et al. 2019). The similarity between the flaring in J1820 and J1910.2 suggests that J1910.2 did not undergo state transitions during its re-flaring, a conclusion also reached by Saikia et al. (2023a). The late time radio increases from MAXI J1348−630 appear to have roughly the same spacing as for J1820, and while they are less well-sampled their shapes are consistent (Carotenuto et al. 2021a). Finally, Chen, Shrader & Livio (1997) present a large sample of X-ray light curves from X-ray novae, with the source XN 0422+32 showing similar flaring to J1820.

In the case of J1820 the similarity of R1/R2/R3 to R0 indicates that the morphology of the rebrightening events can occur during the canonical outburst. The rebrightening events themselves show some similarity to those predicted from disc instability models where irradiation heating from the inner accretion disc (or corona) is included (Dubus, Hameury & Lasota 2001). In this model the length of the flare is set by the strength of the irradiation and the disc mass transfer rate, whereas the profile is set by an initial exponential decay where the hot disc is kept fully ionized and no cooling front can form, followed by a cooling front that moves inwards due to weakening irradiation. Finally, once the irradiation level drops significantly enough, the evolution continues on the thermal time-scale (Dubus et al. 2001; Tetarenko et al. 2018a). From an observational perspective this should result in a disc light curve profile described by a sharp rise, followed by a decaying phase which switches to a steeper day during the decline. This is morphologically consistent with the light curves shown in Fig. 8, with a slow linear (in the log–linear plot) decay followed by a more rapid decline. Even though these radio light curves are probing the core jet, a similar profile is seen in the radio and optical.

Finally, we check for evidence of changes in the X-ray–radio correlation during the evolution of the rebrightening events. Despite the clear change in decay rate seen at ~ 40 d in Fig. 9, we see no indication that the correlation index evolves throughout the rebrightenings, which could have indicated a change in the accretion efficiency (e.g. to an advection dominated accretion flow) during the evolution.

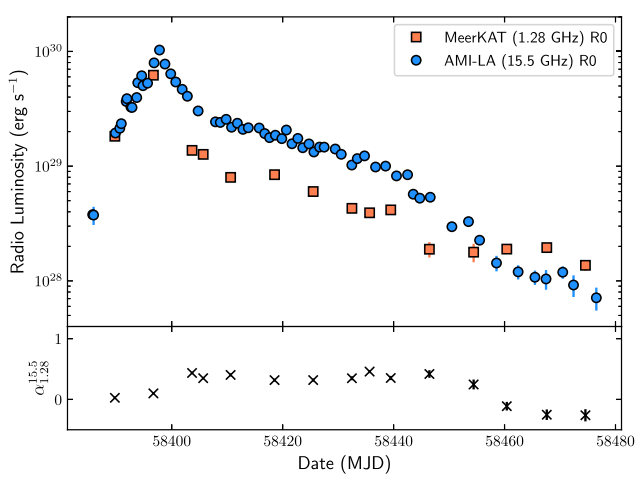

(a) The hard state after J1820 exited the soft state, R0.

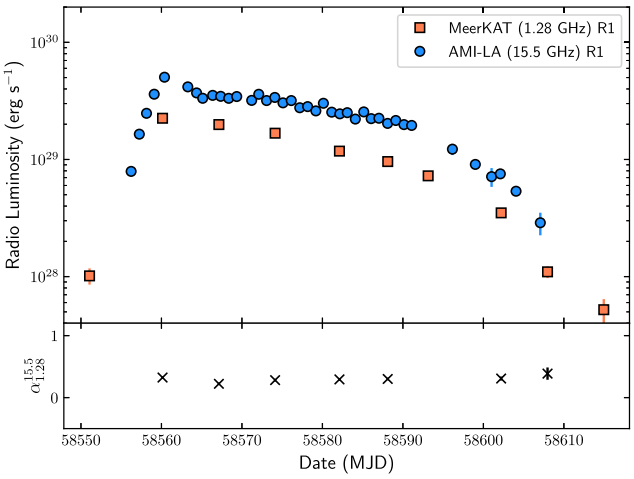

(b) The hard-state only re-brightening event R1.

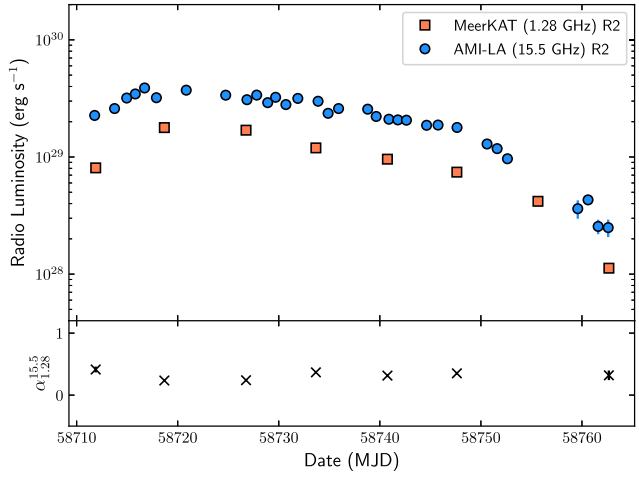

(c) The hard-state only re-brightening event R2.

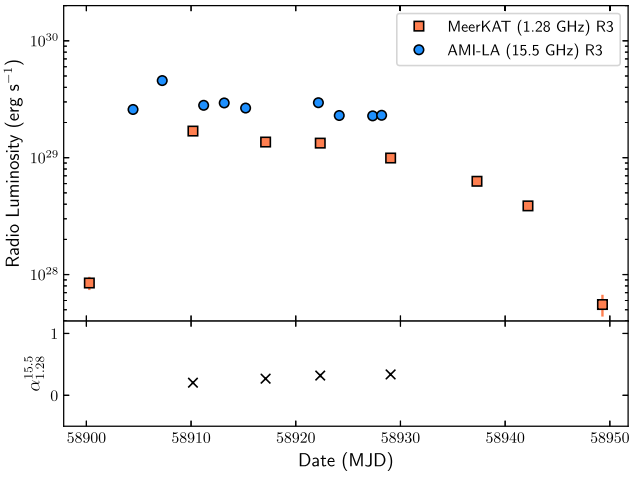

(d) The hard-state only re-brightening event R3.

Figure 8. Light curves and the 1.28 to 15.5 GHz spectral index of the three rebrightening events R1, R2, and R3 (b, c, and d, respectively). Also shown is the hard state that J1820 entered immediately after its only excursion to the soft state (R0; panel a). Note that all plots share the same radio luminosity scale to allow for easier comparison between events.

4.2 Formation of the compact jet

In Fig. 10, we show the transition from the soft to hard state for J1820 with data at radio, optical, and X-ray observing bands. We see an initial hardening of the radio spectrum as the compact core jet re-forms during the intermediate state, while the soft X-rays fade and the optical rises at the end of the intermediate state. The formation of the compact jet is seen in similar detail in Corbel et al. (2013) for GX339−4 (see also Coriat et al. 2009), where the evolution qualitatively matches J1820. It has been suggested that the ordering of the radio/optical rising (which is seen in reverse in the hard to soft state transition) is due to an evolution of the compact/core jet structure where different regions become optically thick on different time-scales (e.g. Miller-Jones et al. 2012; Corbel et al. 2013; Kalemci et al. 2013; Russell et al. 2013b, 2014). This could also be responsible for the drop in optical luminosity that we see during the initial hard state which is evident in Figs 2 and 6, with the ordering reversed (the region of the jet closest to the black hole quenching before those at larger radii; Coriat et al. 2009; Yan & Yu 2012; Russell et al. 2020).

4.3 Jet contribution to optical emission

It is well known that during the hard to soft state transition in BHXRBs the core jet is significantly quenched (Fender et al. 1999b; Russell et al. 2019b; Bright et al. 2020) or switches off entirely. This is most readily seen in high-angular resolution and sensitivity radio observations, which can distinguish any contamination from the launch of transient ejecta (Bright et al. 2020; Wood et al. 2021). The state transition is also associated with a change in the configuration of the inner accretion disc, responsible for the X-ray emission, with the peak of the X-ray shifting to $\sim$ 1 keV. This can be seen in Fig. 2 where the soft X-ray luminosity as measured by *Swift* rises as J1820 enters the soft state. From Fig. 6, we see a clear signature of optical quenching before the source entered the hard to soft intermediate state. The quenching is significant, about 1 dex, and precedes a large drop in the radio flux density. The drop from MJD $\sim$ 58200 to MJD $\sim$ 58230 is likely to be at least partly caused by the optical emission from the jet quenching before the radio as the spectrum 'collapses' from higher to lower frequencies. In this scenario the remaining optical emission is therefore produced by remaining

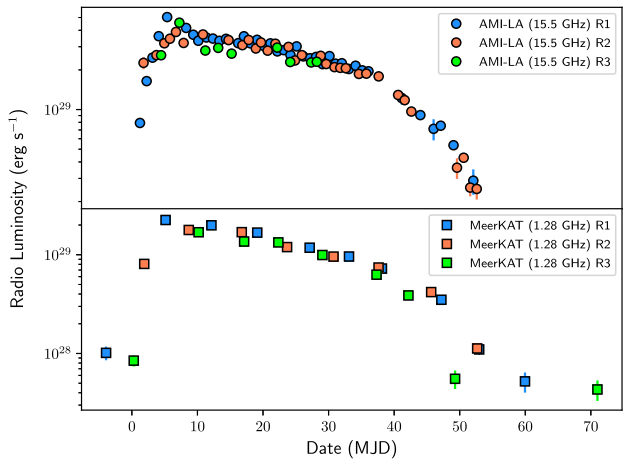

Figure 9. The three hard-state-only rebrightenings shown by J1820 (blue, red, and green, chronologically), as seen at 1.28 GHz (squares) at 15.5 GHz (circles). The rebrightenings have been shifted in time to overlap the first rebrightening in order to demonstrate their regularity. The second and third rebrightenings have been shifted by 155 and 365 d, respectively. Denoting the start time of rebrightening episode RX as $t_{\rm RX}$ these offsets imply $t_{\rm R2} - t_{\rm R1} = 155$ d and $t_{\rm R3} - t_{\rm R2} = 190$ d.

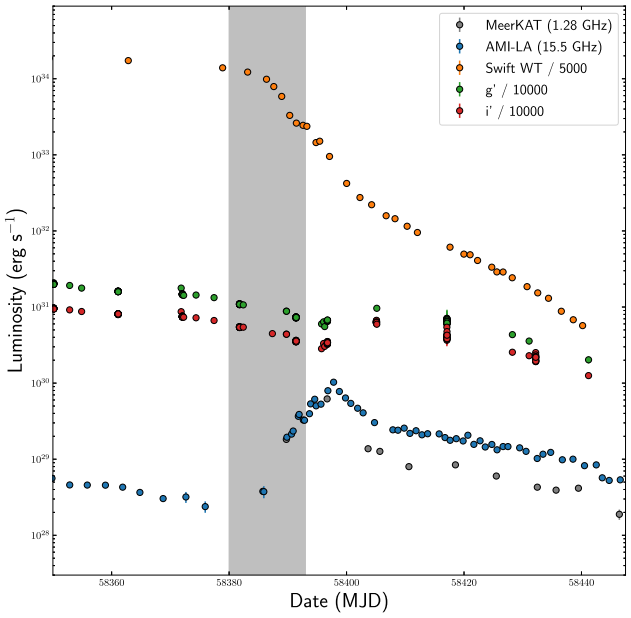

Figure 10. The soft to hard state transition showing the re-ignition of the core jet, particularly obvious at radio frequencies. The X-ray and optical luminosities have been scaled down by a factor of 5000 and 10 000, respectively, to ease comparison.

sources of optical emission, most likely dominated by the accretion disc (both directly, and through reprocessing). This is consistent with the broadband SED modelling performed in Echiburú-Trujillo et al. 2024 (the optical fading is also discussed in the context of the optical/X-ray correlation in Yang et al. 2025).

The expected correlation between optical and radio emission depends on the emission mechanism primarily responsible for the production of optical photons. While radio emission from hard state BHXRBs is well established to be produced in a compact jet, the optical emission is likely some combination of outer disc photons, reprocessed inner disc photons, and photons from a region of the jet closer to the black hole than the ones responsible for the radio emission (the companion star is sub-dominant, see e.g. Echiburú-Trujillo et al. 2024). Russell et al. (2006) showed that the optical–X-ray correlation in the soft state was mostly unchanged when compared to the hard state, whereas the infrared was significantly suppressed compared to the X-rays, indicating that the jet is contributing near-infrared (NIR) photons which are quenched along with the radio in the soft state. It is likely that any optical jet emission is above the jet break frequency where the jet synchrotron emission becomes optically thin, as shown by Echiburú-Trujillo et al. (2024) for J1820, and so the relative contribution will be suppressed when compared to NIR and therefore the impact on the light curves more subtle.

In the case that the optical emission is primarily caused by the reprocessing of inner disc X-ray photons, a theoretical correlation between the two components of $L_{\rm O} \propto L_{\rm X}^{0.5} a$ is expected (van Paradijs & McClintock 1994), where a is the orbital separation of the system (which remains constant for well circularized binaries). Coupling this with the radio X-ray correlation of $L_{\rm R} \propto L_{\rm X}^{\sim 0.6}$, well established for radio-loud black hole X-ray binaries in the hard state (and consistent with originating from a radiatively inefficient accretion flow; e.g. Narayan & Yi 1995; Körding, Fender & Migliari 2006), gives the prediction $L_{\rm O} \propto L_{\rm R}^{\sim 0.8}$, entirely consistent with the correlations shown in Fig. 6 for J1820 when adjusting for the shallower radio–X-ray correlation found for this source. Note that this correlation holds well using radio measurements an order of magnitude different in frequency, and for multiple optical bands (although the errors on the MeerKAT–optical observation are significantly larger than for the AMI-LA–optical correlation).

If instead optical emission is produced primarily in the jet, and the optical and radio emission are both produced as part of the same power-law components on the spectrum (e.g. the flat self-absorbed core spectrum[3]) then, of course, $L_{\rm O} \propto L_{\rm R}$ is expected, with the same correlation between X-ray and optical emission as between X-ray and radio emission. This scenario is indistinguishable from the reprocessing model due to the flatter radio–X-ray correlation for J1820 and so based on correlation arguments no conclusions can be drawn on the presence of optical photons. We note that the optical–X-ray correlations shown in Fig. 5 have a marginally shallower index than expected for the model of Paradijs & McClintock (1994).

4.4 The radio–X-ray correlation

The radio–X-ray correlation is a widely used diagnostic for accreting systems, probing the connection between accretion and the process of jet production and propagation. Active galactic nuclei (AGNs) and a sub-set of the X-ray binaries lie on the Fundamental Plane of black hole activity, showing $L_{\rm R} \propto L_{\rm X}^{0.6}$ when marginalizing over the black hole mass (Merloni, Heinz & di Matteo 2003; Falcke, Körding & Markoff 2004). The observations presented in this work, and in Bright et al. (2020), mark J1820 as one of the best sampled sources in the radio–X-ray plane, second only to GX 339−4 (e.g. Corbel et al. 2003; Tremou et al. 2020). The best correlation we find for J1820 of $a = 0.482 \pm 0.007$ is shallower than for the Fundamental Plane of black hole activity, however J1820 is clearly similar to the radio-loud sources for the entirety of its outburst in terms of radio luminosity. Sharp deviations from the radio–X-ray correlation can be seen when

[3]Or even if the optical is in the optically thin synchrotron regime, since the jet spectral break does not shift dramatically in frequency at different luminosities in the hard state (Russell et al. 2013a).

the source transitions between the hard and soft accretion states, with a return to the correlation from the reverse transition. This behaviour tracks the quenching and re-ignition of the core jet. Radio detections in the soft state have been unambiguously associated with the presence of transient ejecta no longer connected to the accretion processes close to the black hole (Bright et al. 2020; Espinasse et al. 2020; Wood et al. 2021).

The high density of our sampling at X-ray and radio wavelengths allows us to test for possible changes in the correlation over the outburst. It has been suggested (Coriat et al. 2011) that the correlation index can be directly associated with the efficiency of accretion on to the compact object, with the radio loud and radio quiet corresponding to inefficient and efficient accretion states, respectively. Radio-quiet sources rejoin the loud track at low luminosities, possibly indicating a switch in accretion efficiency. Radio-loud sources seem to never deviate from the track, although the correlation for J1820 is shallower than the canonical slope. For J1820 there appears to be a flattening in the radio X-ray correlation to $a = 0.35 \pm 0.02$ when the X-ray luminosity is between $\sim 10^{35}$ and $\sim 10^{36}$ erg s^{-1} for both the fading hard state and the rebrightenings, occurring in a similar luminosity range to that seen for radio-quiet sources as they rejoin the radio-loud track (e.g. Carotenuto et al. 2021b). It has also been suggested that a shallower radio–X-ray correlation is a feature of hard-state only outbursts from GX 339−4, which de Haas et al. (2021) suggest could be driven by a different coupling between the jet and the accretion flow in these outbursts. It should be noted that while individual sources clearly traverse different paths in the radio–X-ray plane, the existence of two distinct tracks is disputed, as is any difference in the correlation index for BHs and neutron stars (Gallo, Degenaar & van den Eijnden 2018). Any such difference would be an important consideration for models attempting to explain the radio–X-ray correlation using accretion efficiency (see e.g. Gusinskaia et al. 2020; Gasealahwe et al. 2023).

4.5 A three-dimensional activity plane

The creation of a three dimensional radio–optical–X-ray activity plane for J1820 provides a full picture of its evolution. It is clear that during the hard state the three wavelengths are tightly coupled (unsurprisingly, given Fig. 2), apart from during the rising hard state where the optical faded independently. The hysteresis pattern regularly seen in the radio–X-ray correlation plane is present also in three dimensions, with the optical rejoining the radio–optical–X-ray correlation at a lower luminosity. The fading hard state and three rebrightening events are indistinguishable in this space. A fully interactive version of this figure is available at https://joesbright.github.io/MAXIJ180.

5 CONCLUSIONS

We present high temporal density radio, X-ray, and optical monitoring observations of the black hole X-ray binary MAXI J1820 over more than 4 yr (from 2018 March 12 to 2022 August 01), beginning with its first recorded outburst and including multiple rebrightening events. These data are among the most comprehensive that exist for a BHXRB at these wavelengths. We have constructed all possible correlations between these three observing bands, including the three-dimensional activity plane, providing new insights into the evolution of XRB outbursts. Particularly, we see that during the rising hard state the radio and X-ray emission are strongly coupled and relatively stable, while the optical emission decays significantly. We speculate that this could be the result of the compact jet quenching from its base and then gradually to larger size scales down the flow. During the soft to hard state transition we see peaks in the radio and optical emission ordered in reverse when compared to the hard to soft transition. In the fading hard state, and subsequent rebrightenings, the optical emission is well coupled to the X-ray and radio emission at all times. Based on our correlations we are not able to determine the source of the optical jet photons due to a similarity in the predictions for the relationships between optical emission from an irradiated accretion disc and from a flat spectrum jet.

The regularity of the rebrightening events (and to a lesser extent the fading hard state) and their structured morphology bears similarities to those predicted by extensions to the disc instability model that include irradiation heating from the central accretion disc. Particularly, we see an exponential decay followed by a sharper decline, which are controlled by the viscous time-scale and cooling time-scales, respectively (Dubus et al. 2001; Tetarenko et al. 2018a,b).

For sources with appropriately sampled data the formation of a radio–optical–X-ray plane allows for a better understanding of the complex interplay between accretion and jet production. This is particularly important for the optical emission, which has contributions from both the accretion disc and the jet. In the near future the formation of the radio–optical–X-ray plane should be possible for the bright BHXRB *Swift* J1727.8–1613, which has exceptional radio coverage (Hughes et al. 2025).

ACKNOWLEDGEMENTS

We thank Dan Bramich for the development of the XB-NEWS pipeline used for extracting the optical LCO magnitudes. RF acknowledges support from UKRI, The European Research Council, and the Hintze Charitable Foundation. JvdE was supported by funding from the European Union's Horizon Europe research and innovation programme under the Marie Skłodowska-Curie grant agreement No. 101148693 (MeerSHOCKS), and acknowledges a Warwick Astrophysics prize post-doctoral fellowship made possible thanks to a generous philanthropic donation and a Lee Hysan Junior Research Fellowship awarded by St. Hilda's College, Oxford. We thank the staff at the Mullard Radio Astronomy Observatory for carrying out observations with the AMI-LA. The MeerKAT telescope is operated by the South African Radio Astronomy Observatory (SARAO), which is a facility of the National Research Foundation, an agency of the Department of Science and Innovation. We thank the SARAO staff for conducting these observations. We acknowledge the use of the ilifu cloud computing facility – www.ilifu.ac.za, a partnership between the University of Cape Town, the University of the Western Cape, the University of Stellenbosch, Sol Plaatje University, the Cape Peninsula University of Technology, and the South African Radio Astronomy Observatory. The ilifu facility is supported by contributions from the Inter-University Institute for Data Intensive Astronomy (IDIA – a partnership between the University of Cape Town, the University of Pretoria, and the University of the Western Cape), the Computational Biology division at UCT and the Data Intensive Research Initiative of South Africa (DIRISA). This work makes use of observations from the Las Cumbres Observatory global telescope network. We acknowledge the use of public data from the *Swift* data archive. This work made use of data supplied by the UK Swift Science Data Centre at the University of Leicester. This material is based upon work supported by Tamkeen under the NYU Abu Dhabi Research Institute grant CASS. This work benefited from discussions during Team Meetings of the International Space Science Institute (Bern), whose support we acknowledge. We thank

the anonymous referee for their comments, which helped improve this manuscript.

DATA AVAILABILITY

All data presented in this work are provided in machine readable format as part of the online version of the paper. Radio and optical images from which flux densities were derived are available upon reasonable request to the corresponding author. *Swift* data products can be recreated from the public data archive and using XSPEC in HEASOFT.

REFERENCES

Alabarta K. et al., 2021, MNRAS, 507, 5507
Arnaud K. A., 1996, in Jacoby G. H., Barnes J., eds, ASP Conf. Ser. Vol. 101, Astronomical Data Analysis Software and Systems V. Astron. Soc. Pac., San Francisco, p. 17
Atri P. et al., 2020, MNRAS, 493, L81
Baglio M. C., Russell D. M., Alabarta K., Saikia P., Bramich D. M., Homan J., Lewis F., 2023, Astron. Telegram, 16192
Baglio M. C., Russell D. M., Lewis F., 2018, Astron. Telegram, 11418
Baglio M. C., Russell D. M., Saikia P., Bramich D. M., Lewis F., 2021, Astron. Telegram, 14492
Bahramian A. et al., 2023, ApJ, 948, L7
Belloni T. M., 2010, in Belloni T., ed., Lecture Notes in Physics. Springer Verlag, Berlin, p. 53
Blandford R. D., Königl A., 1979, ApJ, 232, 34
Bramich D. M., Freudling W., 2012, MNRAS, 424, 1584
Briggs D. S., 1995, PhD thesis, New Mexico Institute of Mining and Technology
Bright J. S. et al., 2020, Nat. Astron., 4, 697
Burrows D. N. et al., 2005, Space Sci. Rev., 120, 165
Cardelli J. A., Clayton G. C., Mathis J. S., 1989, ApJ, 345, 245
Carotenuto F. et al., 2021a, MNRAS, 504, 444
Carotenuto F. et al., 2021b, MNRAS, 505, L58
Carotenuto F., Corbel S., Tzioumis A., 2022, MNRAS, 517, L21
CASA Team, 2022, PASP, 134, 114501
Chaty S., Haswell C. A., Malzac J., Hynes R. I., Shrader C. R., Cui W., 2003, MNRAS, 346, 689
Chen W., Shrader C. R., Livio M., 1997, ApJ, 491, 312
Corbel S. et al., 2001, ApJ, 554, 43
Corbel S. et al., 2013, MNRAS, 431, L107
Corbel S., Fender R. P., 2002, ApJ, 573, L35
Corbel S., Fender R. P., Tzioumis A. K., Nowak M., McIntyre V., Durouchoux P., Sood R., 2000, A&A, 359, 251
Corbel S., Fender R. P., Tzioumis A. K., Tomsick J. A., Orosz J. A., Miller J. M., Wijnands R., Kaaret P., 2002, Science, 298, 196
Corbel S., Nowak M. A., Fender R. P., Tzioumis A. K., Markoff S., 2003, A&A, 400, 1007
Coriat M. et al., 2011, MNRAS, 414, 677
Coriat M., Corbel S., Buxton M. M., Bailyn C. D., Tomsick J. A., Körding E., Kalemci E., 2009, MNRAS, 400, 123
Cúneo V. A. et al., 2020, MNRAS, 496, 1001
Cunningham C., 1976, ApJ, 208, 534
Davies M. L. et al., 2009, MNRAS, 400, 984
de Haas S. E. M. et al., 2021, MNRAS, 502, 521
Denisenko D., 2018, Astron. Telegram, 11400
Dhawan V., Mirabel I. F., Rodríguez L. F., 2000, ApJ, 543, 373
Dubus G., Hameury J. M., Lasota J. P., 2001, A&A, 373, 251
Echiburú-Trujillo C. et al., 2024, ApJ, 962, 116
Espinasse M. et al., 2020, ApJ, 895, L31
Evans P. A. et al., 2009, MNRAS, 397, 1177
Falcke H., Biermann P. L., 1995, A&A, 293, 665
Falcke H., Körding E., Markoff S., 2004, A&A, 414, 895
Fender R. et al., 1999b, ApJ, 519, L165
Fender R. et al., 2016, preprint (arXiv:1711.04132)
Fender R. P., Belloni T. M., Gallo E., 2004, MNRAS, 355, 1105
Fender R. P., Garrington S. T., McKay D. J., Muxlow T. W. B., Pooley G. G., Spencer R. E., Stirling A. M., Waltman E. B., 1999a, MNRAS, 304, 865
Gallo E., Degenaar N., van den Eijnden J., 2018, MNRAS, 478, L132
Gallo E., Fender R. P., Hynes R. I., 2005, MNRAS, 356, 1017
Gallo E., Miller B. P., Fender R., 2012, MNRAS, 423, 590
Gasealahwe K. V. S. et al., 2023, MNRAS, 521, 2806
Gehrels N. et al., 2004, ApJ, 611, 1005
Goodwin A. J. et al., 2020, MNRAS, 498, 3429
Gusinskaia N. V. et al., 2020, MNRAS, 492, 2858
Heywood I., 2020, Astrophysics Source Code Library, record ascl:2009.003
Hickish J. et al., 2018, MNRAS, 475, 5677
Homan J. et al., 2020, ApJ, 891, L29
Homan J., Belloni T., 2005, Ap&SS, 300, 107
Homan J., Buxton M., Markoff S., Bailyn C. D., Nespoli E., Belloni T., 2005, ApJ, 624, 295
Hughes A. et al. . preprint (arXiv:2506.07798)
Hugo B. V., Perkins S., Merry B., Mauch T., Smirnov O. M., 2022, in Ruiz J. E., Pierfedereci F., Teuben P., eds, ASP Conf. Ser. Vol. 532, Astronomical Data Analysis Software and Systems XXX. Astron. Soc. Pac., San Francisco, p. 541
Kalemci E., Dinçer T., Tomsick J. A., Buxton M. M., Bailyn C. D., Chun Y. Y., 2013, ApJ, 779, 95
Kara E. et al., 2019, Nature, 565, 198
Kawamuro T. et al., 2018, Astron. Telegram, 11399
Kennea J. A., Marshall F. E., Page K. L., Palmer D. M., Siegel M. H., Neil Gehrels Swift Observatory Team, 2018, Astron. Telegram, 11403
Kenyon J. S., Smirnov O. M., Grobler T. L., Perkins S. J., 2018, MNRAS, 478, 2399
Kochanek C. S. et al., 2017, PASP, 129, 104502
Koljonen K. I. I., Long K. S., Matthews J. H., Knigge C., 2023, MNRAS, 521, 4190
Körding E. G., Fender R. P., Migliari S., 2006, MNRAS, 369, 1451
Lewis F., 2018, Robotic Telescope, Student Research and Education Proceedings, 1, 233
Lewis F., Russell D. M., Fender R. P., Roche P., Clark J. S., 2008, preprint (arXiv:0811.2336)
Ma R., Méndez M., García F., Sai N., Zhang L., Zhang Y., 2023, MNRAS, 525, 854
Ma X. et al., 2021, Nat. Astron., 5, 94
Maccarone T. J., Osler A., Miller-Jones J. C. A., Atri P., Russell D. M., Meier D. L., McHardy I. M., Longa-Peña P. A., 2020, MNRAS, 498, L40
Makhathini S., 2018, PhD thesis, Rhodes University, South Africa
Matsuoka M. et al., 2009, PASJ, 61, 999
McCully C., Volgenau N. H., Harbeck D.-R., Lister T. A., Saunders E. S., Turner M. L., Siiverd R. J., Bowman M., 2018, in Guzman J. C., Ibsen J., eds, Proc. SPIE Conf. Ser. Vol. 10707, Software and Cyberinfrastructure for Astronomy V. SPIE, Bellingham, p. 107070K
McMullin J. P., Waters B., Schiebel D., Young W., Golap K., 2007, in Shaw R. A., Hill F., Bell D. J., eds, ASP Conf. Ser. Vol. 376, Astronomical Data Analysis Software and Systems XVI. Astron. Soc. Pac., San Francisco, p. 127
Merloni A., Heinz S., di Matteo T., 2003, MNRAS, 345, 1057
Migliori G., Corbel S., Tomsick J. A., Kaaret P., Fender R. P., Tzioumis A. K., Coriat M., Orosz J. A., 2017, MNRAS, 472, 141
Mihara T. et al., 2011, PASJ, 63, S623
Miller-Jones J. C. A. et al., 2012, MNRAS, 421, 468
Mirabel I. F., Rodríguez L. F., 1994, Nature, 371, 46
Motta S. E., Casella P., Fender R. P., 2018, MNRAS, 478, 5159
Muñoz-Darias T. et al., 2019, ApJ, 879, L4
Narayan R., Yi I., 1995, ApJ, 452, 710
Offringa A. R. et al., 2014, MNRAS, 444, 606
Özbey Arabacı M., Kalemci E., Dinçer T., Bailyn C. D., Altamirano D., Ak T., 2022, MNRAS, 514, 3894
Paice J. A. et al., 2019, MNRAS, 490, L62
Parikh A. S., Russell T. D., Wijnands R., Miller-Jones J. C. A., Sivakoff G. R., Tetarenko A. J., 2019, ApJ, 878, L28

Perrott Y. C. et al., 2013, MNRAS, 429, 3330
Pirbhoy S. F., Baglio M. C., Russell D. M., Bramich D. M., Saikia P., Yazeedi A. A., Lewis F., 2020, Astron. Telegram, 13451
Plotkin R. M., Bahramian A., Miller-Jones J. C. A., Reynolds M. T., Atri P., Maccarone T. J., Shaw A. W., Gandhi P., 2021, MNRAS, 503, 3784
Plotkin R. M., Gallo E., Jonker P. G., 2013, ApJ, 773, 59
Remillard R. A., McClintock J. E., 2006, ARA&A, 44, 49
Rodriguez J. et al., 2020, ApJ, 889, 58
Russell D. M. et al., 2013a, MNRAS, 429, 815
Russell D. M. et al., 2013b, ApJ, 768, L35
Russell D. M. et al., 2019a, Astron. Nachr., 340, 278
Russell D. M., Baglio M. C., Lewis F., 2019c, Astron. Telegram, 12534
Russell D. M., Fender R. P., Hynes R. I., Brocksopp C., Homan J., Jonker P. G., Buxton M. M., 2006, MNRAS, 371, 1334
Russell T. D. et al., 2019b, ApJ, 883, 198
Russell T. D. et al., 2020, MNRAS, 498, 5772
Russell T. D., Soria R., Miller-Jones J. C. A., Curran P. A., Markoff S., Russell D. M., Sivakoff G. R., 2014, MNRAS, 439, 1390
Saikia P. et al., 2022, ApJ, 932, 38
Saikia P., Russell D. M., Pirbhoy S. F., Baglio M. C., Bramich D. M., Alabarta K., Lewis F., Charles P., 2023a, MNRAS, 524, 4543
Saikia P., Russell D. M., Pirbhoy S. F., Baglio M. C., Bramich D. M., Alabarta K., Lewis F., Charles P., 2023b, ApJ, 949, 104
Shakura N. I., Sunyaev R. A., 1973, A&A, 24, 337
Shappee B. J. et al., 2014, ApJ, 788, 48
Shaw A. W. et al., 2021, ApJ, 907, 34
Shidatsu M., Nakahira S., Murata K. L., Adachi R., Kawai N., Ueda Y., Negoro H., 2019, ApJ, 874, 183
Staley T. D. et al., 2013, MNRAS, 428, 3114
Stetson P. B., 1990, PASP, 102, 932
Stirling A. M., Spencer R. E., de la Force C. J., Garrett M. A., Fender R. P., Ogley R. N., 2001, MNRAS, 327, 1273
Sugizaki M. et al., 2011, PASJ, 63, S635
Tetarenko A. J. et al., 2021, MNRAS, 504, 3862
Tetarenko A. J., Casella P., Miller-Jones J. C. A., Sivakoff G. R., Tetarenko B. E., Maccarone T. J., Gandhi P., Eikenberry S., 2019, MNRAS, 484, 2987
Tetarenko B. E., Dubus G., Lasota J. P., Heinke C. O., Sivakoff G. R., 2018a, MNRAS, 480, 2
Tetarenko B. E., Lasota J. P., Heinke C. O., Dubus G., Sivakoff G. R., 2018b, Nature, 554, 69
Tetarenko B. E., Sivakoff G. R., Heinke C. O., Gladstone J. C., 2016, ApJS, 222, 15
Tonry J. L. et al., 2018, ApJ, 867, 105
Torres M. A. P., Casares J., Jiménez-Ibarra F., Álvarez-Hernández A., Muñoz-Darias T., Armas Padilla M., Jonker P. G., Heida M., 2020, ApJ, 893, L37
Torres M. A. P., Casares J., Jiménez-Ibarra F., Muñoz-Darias T., Armas Padilla M., Jonker P. G., Heida M., 2019, ApJ, 882, L21
Tremou E. et al., 2020, MNRAS, 493, L132
Tucker M. A. et al., 2018, ApJ, 867, L9
van Paradijs J., McClintock J. E., 1994, A&A, 290, 133
Veledina A. et al., 2019, A&A, 623, A75
Veledina A., Poutanen J., Vurm I., 2013, MNRAS, 430, 3196
Vincentelli F. M. et al., 2021, MNRAS, 503, 614
Vrtilek S. D., Raymond J. C., Garcia M. R., Verbunt F., Hasinger G., Kurster M., 1990, A&A, 235, 162
Wang J. et al., 2021, ApJ, 910, L3
Williams D. R. A. et al., 2020, MNRAS, 491, L29
Wood C. M. et al., 2021, MNRAS, 505, 3393
Wood C. M. et al., 2024, ApJ, 971, L9
Yan Z., Yu W., 2012, MNRAS, 427, L11
Yang P. et al., 2025, preprint (arXiv:2507.00532)
You B. et al., 2021, Nat. Commun., 12, 1025
Zwart J. T. L. et al., 2008, MNRAS, 391, 1545

SUPPORTING INFORMATION

Supplementary data are available at *MNRAS* online.

suppl_data

Please note: Oxford University Press is not responsible for the content or functionality of any supporting materials supplied by the authors. Any queries (other than missing material) should be directed to the corresponding author for the article.

This paper has been typeset from a TEX/LATEX file prepared by the author.